UNIVERSITY *of York*

This is a repository copy of *First Principles Investigation of the Structure and Properties of Au Nanoparticles Supported on ZnO*.

White Rose Research Online URL for this paper:
https://eprints.whiterose.ac.uk/149211/

Version: Published Version

Article:

White Rose
university consortium
Universities of Leeds, Sheffield & York

eprints@whiterose.ac.uk
https://eprints.whiterose.ac.uk/

First-Principles Investigation of the Structure and Properties of Au Nanoparticles Supported on ZnO

Shih-Hsuan Hung* and Keith McKenna*

Department of Physics, University of York, Heslington, York YO10 5DD, United Kingdom

Ⓢ *Supporting Information*
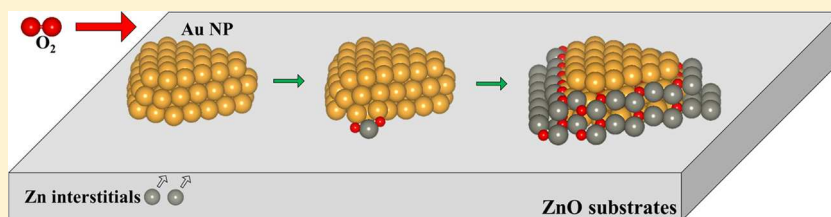
ABSTRACT: We present a first-principles investigation of the structure, stability, and reactivity of Au nanoparticles (NPs) supported on ZnO. The morphologies of supported Au NPs are predicted using the formation energy of Au surfaces and the adhesion energy between Au and the dominant ZnO surfaces exposed on ZnO tetrapods. We show how Zn interstitials (a stable intrinsic defect in ZnO) are attracted toward the Au/ZnO interface and in the presence of oxygen can lead to the encapsulation of Au by ZnO, an effect that is observed experimentally. We find that O_2 molecules absorb preferentially at the perimeter of the NP in contact with the ZnO support. These results provide atomistic insight into the structure of ZnO-supported Au NPs with relevance to CO oxidation.

1. INTRODUCTION

Au nanoparticles (NPs) supported on ZnO are attractive for a wide range of catalytic applications including CO oxidation,[1−9] selective hydrogenation of aldehydes,[10−12] oxidation of salicylic alcohols,[13] photoelectrochemial water splitting[14] and photocatalytic degradation of dyes.[15,16] As a support, ZnO also offers exciting opportunities to tune porosity, optical, chemical, and mechanical properties through the synthesis of tailored ZnO tetrapods and other low-dimensional morphologies.[17−24] Au NPs supported on ZnO tetrapods have been shown to provide very high catalytic performance for CO oxidation compared to other catalytic systems.[5,6,25] Transmission electron microscopy (TEM) imaging suggests that annealing in the presence of oxygen can lead to the encapsulation of Au NPs by ZnO and a reduction of activity.[26] However, the mechanism behind this effect remains unclear. Although Au NPs on various oxide supports (including MgO, TiO_2, CeO_2, and Fe_2O_3[1−4]) have been studied extensively by first-principles calculations, Au/ZnO tetrapod systems remain relatively unexplored. Together with the fact that direct information on atomic scale structure and chemical properties of these systems are challenging to obtain means that the current understanding of the structure and chemical properties of ZnO-supported Au NPs is fairly limited.

In this article, we present a density functional theory (DFT) investigation into the structure and properties of Au NPs supported on ZnO. To predict the morphology of Au NPs, we first determine the atomic structures and adhesion energies for all possible interfaces between the three low-index surfaces of Au and the two surfaces exposed on ZnO tetrapods.[17,26,27]

Together with the calculated formation energies of Au surfaces, we then obtain the equilibrium NP morphology using the Wulff−Kaichew construction.[28] By constructing explicit atomic scale models of the most stable supported Au NPs, we investigate their interaction with oxygen. We show how Zn interstitials (a stable intrinsic defect in ZnO) are attracted toward the Au/ZnO interface and in the presence of oxygen can form ZnO monomers, which attach at the perimeter of the NP, suggesting a mechanism for the ZnO encapsulation observed experimentally. We find that O_2 molecules absorb on both the exposed Au facets as well as the perimeter of the NP (coordinating to both Au atoms and a Zn atom in the support) with the latter being more stable. These results provide atomistic insight into the structure and properties of ZnO-supported Au NPs with relevance to CO oxidation.

2. BACKGROUND

Wurtzite ZnO has lattice constants of $a = 3.24$ and $c/a = 1.60$ and a band gap of 3.44 eV.[29,30] O vacancies and interstitials (octahedral site) are the most stable point defects in ZnO leading to intrinsic *n*-type conductivity.[31] DFT calculations using local or semilocal exchange−correlation (XC) functionals provide a reasonable description of the structure of ZnO (e.g., $a = 3.20$ and $c/a = 1.61$ using LDA[32,33]) but lead to a significant underestimation of the band gap.[34] Hybrid functional approximations to XC (such as the HSE functional)

give much more accurate predictions of the band gap (3.2 eV) and also properties of point defects.[35,36] There have been many experimental studies of the electronic properties of defects in ZnO using techniques such as electron paramagnetic resonance and photoluminescence spectroscopy.[31,37−39] The consistent picture that emerges from the experiment and hybrid functional DFT calculations is that the O vacancy is a deep donor with a defect level located around 1 eV below the conduction band minimum,[36,40] and the interstitial is a shallow donor with approximately 0.05 eV ionization energy.[31,35,36,39] However, hybrid DFT approaches are computationally very expensive and less suited to modeling systems, which contain metallic components (such as supported metal NPs). An alternative is provided by the combination of the GGA + U approach together with nonlocal external potentials (GGA + NLEP + U), which has been shown to give an accurate description of both the crystal structure and band gap for ZnO (a = 3.20, c/a = 1.58, and E_g = 3.23 eV) but at a much reduced computational cost compared to hybrid functional approaches.[41−44]

A wide range of ZnO nanostructures including nanocombs, nanorings, nanobelts, and nanorods can be synthesized using solvothermal, chemical vapor deposition, and solid−vapor thermal sublimation approaches.[17,27,45,46] Nanorods are typically elongated in the [0001] direction, hexagonal in cross-section, and expose {10$\bar{1}$0} and {11$\bar{2}$0} surfaces along their length.[18,26,27,47] Nanorods can be arranged into different hierarchical structures offering opportunities to tailor for specific applications. ZnO tetrapods (nanosized rod-shaped ZnO crystals joined to form a tetrahedron) are particularly well studied and have been used as a support for Au NPs for catalytic applications (discussed below). X-ray diffraction shows that ZnO nanorods (including tetrapod morphologies) have a wurtzite crystal structure.

Au NPs have been extremely well studied experimentally and theoretically, both unsupported and supported on various oxide supports.[25,48−50] The experimental lattice constant of face-centered cubic (fcc) Au is 4.08 Å, and a slightly larger lattice constant is usually obtained by DFT calculations.[51,52] The three most stable surfaces of the Au fcc structure are (100), (110), and (111) leading to a truncated-octahedral equilibrium crystal shape.[53] The structure of Au NPs on various oxide supports has been studied theoretically and experimentally.[54,55] Usually, interface structures that maximize the number of Au−O bonds are the most stable. In some cases, oxide supports can induce drastic changes in the morphology of NPs and chemisorption properties, known as the strong metal-support interaction (SMSI).[56−58] For example, encapsulation of Au NPs by TiO$_2$ has been observed on TiO$_2$ substrates under heating.[54] The structure and properties of Au NPs supported on ZnO are less well studied although some electron microscopy investigations show Au NP adsorption along the branches of ZnO tetrapods.[25,26] The observation of the encapsulation of Au NPs supported on ZnO by heating in the presence of O$_2$ is indicative of a SMSI in the Au/ZnO system. However, the origins of the effect are not understood.[26]

There have been a large number of experimental studies demonstrating ZnO-supported Au NPs exhibit high activity for a wide range of oxidation and hydrogenation reactions.[1−6,10−12] The activity for CO oxidation has been found to be around two times that for similar-sized NPs on other supports.[25] For all possible reaction mechanisms, a key step is

the adsorption and dissociation of the O$_2$ molecule, either on the Au NP, at the perimeter in contact with the support or at O vacancy sites in the support. For large unsupported Au NPs, O$_2$ molecules are predicted to adsorb weakly (E_{ads} = −0.08 eV),[59−61] but following dissociation, O atoms relocate to bridge sites where they are adsorbed much more strongly (E_{ads} = −2.54 eV).[61,62] For supported NPs, differences in atomic structure, charge transfer from the support, and the presence of the Au-support interface at the perimeter can lead to significant modification of O$_2$ adsorption and dissociation properties. A few recent theoretical studies have investigated possible reaction mechanisms for small Au clusters (around 10 atoms) supported on ZnO.[63,64] Although the NPs observed in experimental studies are much larger (3−4 nm in diameter), corresponding theoretical models are so far missing.

3. METHODS

First-principles density functional theory (DFT) calculations are performed using the GGA + U method in combination with the nonlocal external potential (NELP) approach using the VASP code.[65,66] The Perdew, Burke, and Ernzerhof (PBE) XC functional is employed.[67] The NELP parameters, which depend on the atomic species and the angular momentum, are as follows: $\Delta V_{Zn,s}$ = +9.4 eV, $\Delta V_{Zn,p}$ = −1.2 eV, $\Delta V_{O,s}$ = −6.4 eV, and $\Delta V_{O,p}$ = −2.0 eV. These NLEP parameters are fitted to reproduce as closely as possible the experimental crystal structure as well as the electronic properties of ZnO by reference to GW calculations. Full details can be found in the following references.[44,68] A U value of +7.0 eV is applied to the d-orbitals of Zn. The Brillouin zone (BZ) is sampled with a Monkhorst−Pack (MP) grid, and the plane-wave basis set is truncated at an energy of 400 eV. The following electrons are treated as valence: Au (6s^1 5d^{10}), Zn (3d^{10} 4p^2), and O (2s^2 2p^4). For the primitive cell calculations (bulk Au and ZnO), a 13 × 13 × 13 MP grid is used for BZ sampling. The calculated lattice constants of ZnO are a = 3.20 Å and c/a = 1.58, and the calculated band gap is 3.20 eV at the Γ-point in reasonable agreement with the experiment. The optimized lattice constant of bulk Au is predicted to be 4.14 Å, which is consistent with other PBE calculations (4.17 Å) and experimental observations (4.08 Å).[52] Tables 1 and 2 summarize the supercells used for all Au/ZnO interfaces and supported Au NP calculations, respectively.

Table 1. Properties of Supercells Used to Model Interfaces Between Au and ZnO Including the Dimensions of Supercells, the Number of Repeated Unit Cells of Au and ZnO, the Lattice Strain Supplied to Au[a]

ZnO(10$\bar{1}$0)	Au(001)	Au(110)	Au(111)
size of the supercell (Å^2)	12.78 × 20.24	3.19 × 20.24	3.19 × 5.06
Au(x, y)	3 × 5	1 × 5 R90	1 × 1
ZnO(x, y)	4 × 5	1 × 4	1 × 1
lattice strain of Au(x, y)	−3%, 3%	−8%, 2%	−9%, 0%
ZnO(11$\bar{2}$0)	Au(001)	Au(110)	Au(111)
size of the supercell (Å^2)	5.53 × 15.18	5.53 × 20.24	5.53 × 5.06
Au(x, y)	2 × 5 R45	2 × 5 R90	2 × 1
ZnO(x, y)	1 × 3	1 × 4	1 × 1
lattice strain of Au(x, y)	5%, −3%	5%, 2%	5%, 0%

[a]All properties are shown for both x- and y-directions.

Table 2. Properties of Supercells Used to Model Au NPs Supported on ZnO Surfaces

	Au$_{NP}$/ZnO(10$\bar{1}$0)	Au$_{NP}$/ZnO(11$\bar{2}$0)
supercell size (Å^3)	28.75 × 25.30 × 23.00	27.66 × 25.30 × 30.00
no. Au atoms	94	67
no. ZnO atoms	540	600

To predict the morphology of the Au NPs using the Wulff–Kaichew construction, we calculate the Au surface formation energies in the following way[28]

$$\gamma = \frac{1}{2A}(E_{\text{tot}} - N\mu) \qquad (1)$$

where A is the cross-sectional area of the surface slab, E_{tot} is the total energy of the surface slab, N is the number of formula units in the surface slab, and μ is the chemical potential of Au (i.e., the total energy per atom in the bulk crystal).

To calculate adhesion energies between Au and ZnO, supercells are constructed containing an interface between Au and ZnO slabs, again with a vacuum gap separating the two free surfaces. The adhesion energy is then calculated in the following way

$$\gamma_{ad} = \frac{1}{A}(E_{Au} + E_{ZnO} - E_{Au/ZnO}) \qquad (2)$$

where $E_{Au/ZnO}$ is the total energy of the optimized Au/ZnO interfacial system and E_{Au} and E_{ZnO} are the total energies of the optimized isolated Au and ZnO slabs.

To assess the stability of point defects at the interface between Au and ZnO surfaces, we calculate the segregation energy defined with respect to the bulk as

$$E_s = E_{\text{interface}}^{\text{d}} - E_{\text{bulk}}^{\text{d}} \qquad (3)$$

where $E_{\text{interface}}^{\text{d}}$ and $E_{\text{bulk}}^{\text{d}}$ represent the total energy of the Au/ZnO system with a point defect at the interface and in the bulk, respectively.

4. RESULTS

4.1. Morphology of Au Nanoparticles. We consider three low-index surfaces, (001), (110), and (111), and calculate their formation energies to predict the equilibrium morphology of the unsupported Au NPs. The dimensions of supercells for (001), (110), and (111) surface calculations are 4.15 × 4.15 × 30.00, 4.15 × 2.93 × 30.00, and 2.93 × 5.08 × 30.00 Å, respectively. These supercells contain a vacuum gap at least 10 Å normal to the surfaces in the z-direction. A 7 × 7 × 1 MP gird is used for BZ sampling to optimize the Au surface structures with 1 k-point in the direction normal to the surfaces. Table 3 summarizes the calculated formation energies of the three optimized Au surfaces. The (111) surface is the most energetically stable surface with γ_{111} = 0.656 J m^{-2},

Table 3. Calculated Surface Formation Energies for the Three Low-Index Surfaces of fcc Au Together with Results from Recent DFT Calculations for Comparison

|	this work	previous works
surface	γ (J m^{-2})	
(001)	0.869	0.873[52]
(110)	0.872	0.900[51]
(111)	0.656	0.734[52]

meanwhile (110) and (001) surfaces show similar formation energies of 0.87 J m^{-2}.

Using the Wulff construction, the predicted morphology of the Au NP is truncated-octahedral (t-Oh) as shown in Figure 1
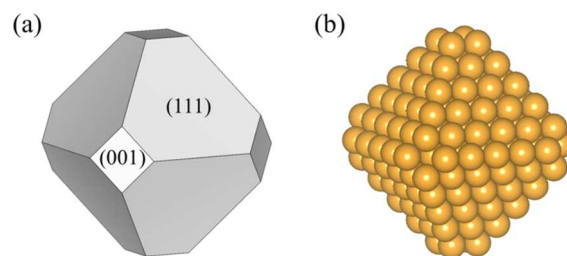
Figure 1. Predicted shape of the unsupported Au t-Oh NP obtained using the Wulff construction. (a) The predicted morphology and (b) an atomic structure consisting of 225 Au atoms.

consisting of six (001) facets and eight (111) facets. The area of the (111) facets accounts for 93 % of the total area. The calculated proportion of the (111) surface is in good agreement with recent theoretical results using standard DFT approaches.[53]

4.2. Structure and Adhesion Energy of Au/ZnO Interfaces. To determine the morphology of Au NPs supported on ZnO surfaces, we calculate the adhesion energy of interfaces between Au and ZnO surfaces. In the interface calculation, we consider (001), (110), and (111) Au surfaces and (10$\bar{1}$0) and (11$\bar{2}$0) ZnO surfaces (which are the common surfaces on ZnO nanorods[18,26,47]). Therefore, there are six different interfaces between the Au and ZnO surfaces. For each, we construct supercells that minimize the strain (the strain is applied to the Au slab in all cases) and determine the most stable structure. The lattice strain applied to the Au surfaces is in the range from 0 to 10% depending on the interface. Figure 2 shows the atomic structure of the most
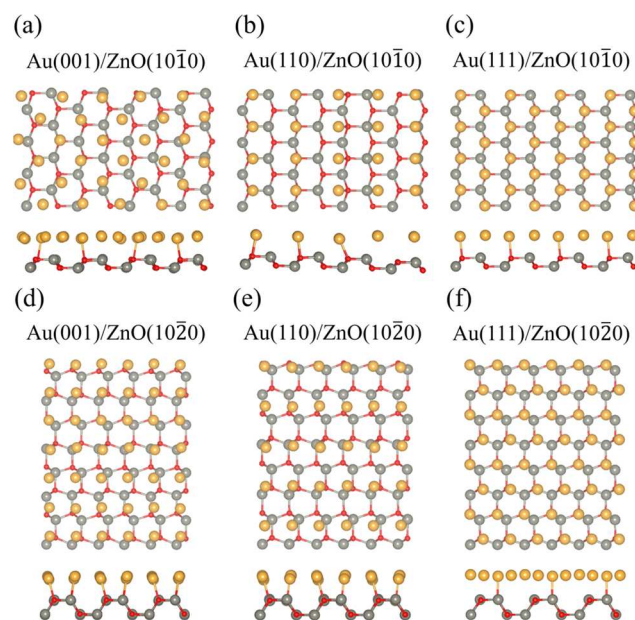
Figure 2. Atomic structure of the interfaces between Au and ZnO surfaces. The upper and lower panels show the top and side views, respectively. The gold, gray, and red spheres represent Au, Zn, and O atoms, respectively.

stable configuration for each interface. In addition, Table 4 summarizes the details of the supercells employed and the key results. Each supercell includes at least 8 layers of ZnO and 8 layers of Au along the z-direction.

Table 4. Adhesion Energies for the Six Different Interfaces between Au and ZnO Surfaces

	ZnO(10$\bar{1}$0)			ZnO(11$\bar{2}$0)		
	Au(001)	Au(110)	Au(111)	Au(001)	Au(110)	Au(111)
E_{ad} (J m^{-2})	0.574	0.717	0.812	0.433	0.421	0.413

The interface between Au(111) and the ZnO(10$\bar{1}$0) surface has the strongest adhesion $E_{ad} = 0.8$ J m^{-2}. The three interfaces between Au and ZnO(11$\bar{2}$0) have similar adhesion energies of around 0.4 J m^{-2}. Due to the lattice mismatch at the interface, the Au atoms of (001) and (110) surfaces are not well aligned to specific sites of the ZnO surfaces. The Au atom can sit on the top of the O, the hollow site of the hexagonal structure and the bridge site of two O atoms. However, for the interfaces between Au(111) and ZnO surfaces, the Au atoms locate directly above the O atoms, as shown in the top view of Figure 2c,f. This Au−O bonding arrangement is more stable and increases the adhesion energy. The similar stable bond formation also has been reported for Au NPs supported on the MgO(001) surface.[55] Besides the pristine surface, we also investigated the influence of O vacancies in the ZnO surfaces on the adhesion energy. We find that an increase in the defect concentration of around 1 nm^{-2} increases the adhesion energy by 0.4 J m^{-2}.

To provide deeper insight, we perform Bader analysis to assess the charge transfer between interface ZnO atoms and Au atoms.[69] In addition, we calculate the vertical distance (l) between Au and ZnO surfaces. Figure 3 shows both vertical
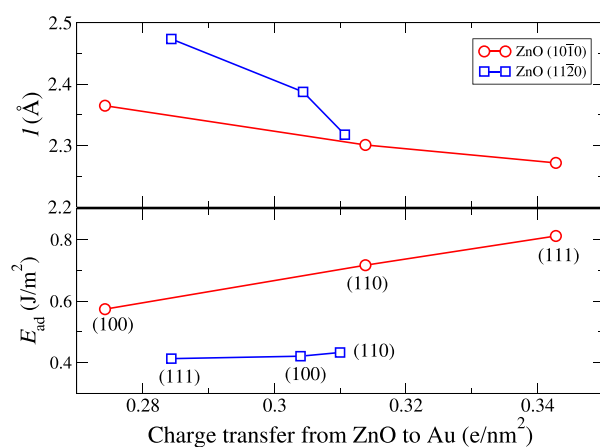

Figure 3. Average separation distance (between Au and ZnO surfaces) l (top) and the adhesion energy E_{ad} (bottom) as a function of the total charge transfer (from ZnO to Au).

distance and adhesion energy as a function of the charge transfer. The trend shows that smaller vertical distance is associated with increased charge transfer and stronger adhesion for both ZnO surfaces. However, the adhesion energy of Au surfaces supported on ZnO(11$\bar{2}$0) is less sensitive to charge transfer compared to interfaces between Au and ZnO(10$\bar{1}$0). We suggest that the difference in sensitivity is due to

differences in the bond formation between interfacial Au atoms and the subsurfaces of the ZnO surfaces. The interplanar distances between the two topmost layers are 0.85 and 1.56 Å for the ZnO(10$\bar{1}$0) and ZnO(11$\bar{2}$0) surfaces, respectively. Consequently, the subsurface of the ZnO(10$\bar{1}$0) has a stronger interaction with the interfacial Au atoms, which further increases the adhesion energy. Therefore, the Au surfaces attach on the ZnO(10$\bar{1}$0) surface with stronger adhesion energy than the ZnO(11$\bar{2}$0) surface.

The predicted morphology of the supported Au NPs is determined using the Wulff−Kaishew construction and is shown in Figure 4. Figure 4a−f represents the Au NPs supported on ZnO(10$\bar{1}$0) and (11$\bar{2}$0) surfaces with different Au facets contacting, respectively. These morphologies show that Au NPs supported on ZnO(11$\bar{2}$0) possess a relatively larger dimension normal to the ZnO surface. To assess the stability of different supported Au NPs, we calculate the total surface free energy

$$E_{TSF} = \sum_{ijk} A_{ijk} \gamma_{ijk} \tag{4}$$

where A_{ijk} and γ_{ijk} represent the area and the formation energy of the specific (ijk) facets, respectively. For the total surface free-energy calculation, we consider a fixed NP volume of 46 nm^3. The total surface free energies of Au nanoparticles in Figure 4a−c are 362, 330, and 265 eV per Au NP, respectively. Meanwhile, the total surface free energy is 376 eV for all Au NPs supported on the ZnO(11$\bar{2}$0) surface. The calculation demonstrates that the total surface free-energy difference between Au NPs supported on the same ZnO surface is less than 0.025 eV per Au atom. Therefore, these three kind of morphologies theoretically survive on both ZnO surfaces. We note that the predicted morphologies are in very good agreement with experimental STEM observations of ZnO-supported Au NPs.[26]

4.3. Au Nanoparticles Supported on ZnO Surfaces. Based on the predicted morphologies above, we construct explicit atomic models of supported Au NPs to study molecular oxygen adsorption. We construct two supercells as shown in Figure 5, one for the most stable morphology on each ZnO surface. The dimensions of the supercells, the number of Au atoms, and the number of ZnO atoms are summarized in Table 5. To prevent the distortion of the ZnO slab during geometry optimization, the coordinates of the bottom layer of the ZnO slab are frozen (6 ZnO layers in total for both slabs). The initial geometry of the interfaces between Au NPs and ZnO surfaces is such that Au atoms are directly located on top of the O atoms. Table 5 also summarizes the calculated adhesion energy, average distance, lattice strain (in the interfacial Au layer), and charge transfer from the ZnO to Au atoms. The calculation shows that the adhesion energy and the vertical distance are reduced compared to the corresponding extended interfaces between Au and ZnO surfaces. The charge transfer is also twice larger than in the slab systems. These results indicate that the interaction between the Au and ZnO surfaces is enhanced for smaller NPs, which may be due to the reduced lattice strain of the interfacial Au atoms (reduced by 4.4 and 3.2% for the ZnO(10$\bar{1}$0) and (11$\bar{2}$0) surfaces, respectively). The average Au−Au bond length of both Au NPs supported on ZnO surfaces is 2.85 Å, which is shorter than the Au−Au bond length in bulk Au (2.93 Å).

Figure 5 also shows the charged state of the supported Au NPs in two orientations (side and bottom views). Bader
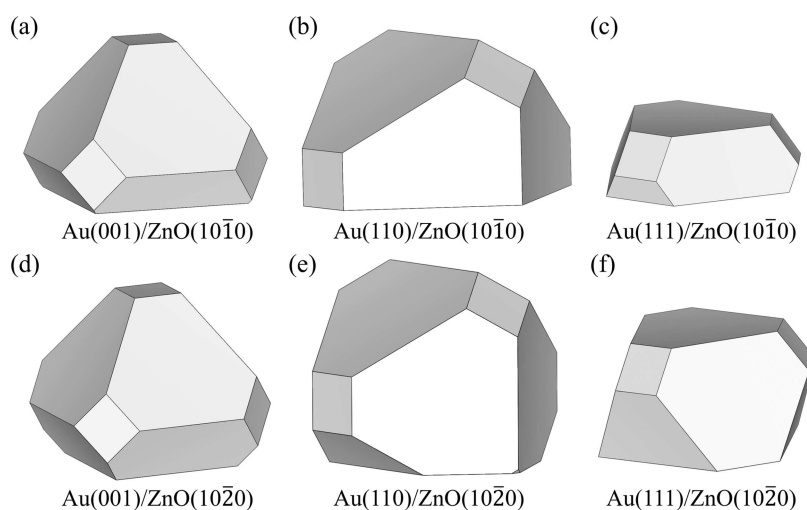
Figure 4. Predicted morphologies of ZnO-supported Au NPs for different orientation relationships (as shown in below panels).
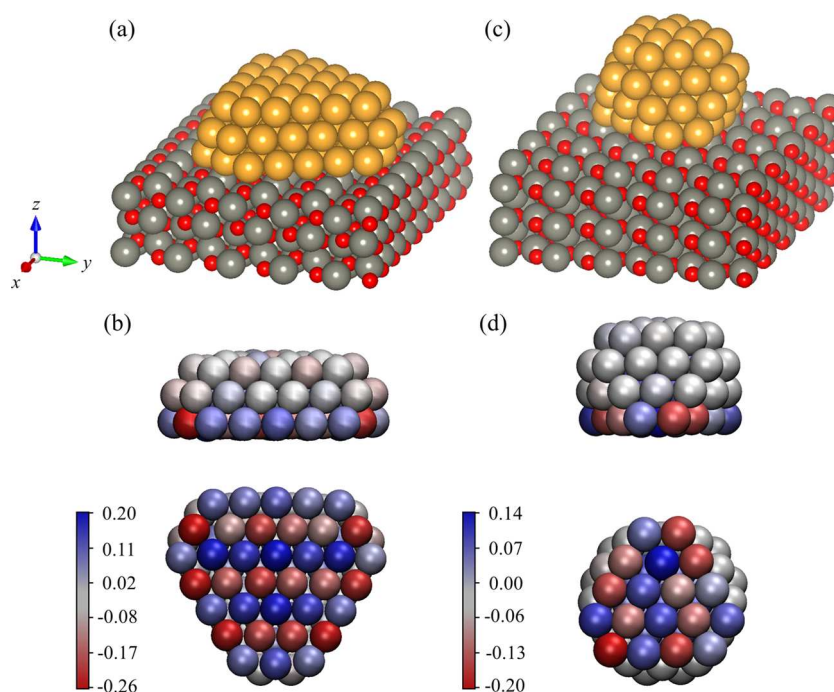

Figure 5. (a) Atomic structure of an Au NP supported on ZnO($10\bar{1}0$). The gold, gray, and red spheres represent the Au, Zn, and O atoms, respectively. (b) Corresponding visualization of the NP (viewed from two different angles) with atoms colored according to their Bader charge. Panels (c) and (d) show the same information for an Au NP supported on ZnO($11\bar{2}0$).

Table 5. Calculated Properties of ZnO-Supported Au NPs

	Au$_{NP}$/ZnO($10\bar{1}0$)	Au$_{NP}$/ZnO($11\bar{2}0$)
γ_{ad} (J m^{-2})	1.16	0.94
avg. distance (Å)	2.29	2.42
avg. lattice strain (%)	4.63	1.81
chg. transfer (e nm^{-2})	0.81	0.79
total chg. transfer (e)	1.46	0.60

analysis indicates that only the interfacial Au atoms are charged (colored in red or blue in Figure 5), with charges between +0.20 and −0.26 e. The positively and negatively charged Au atoms at the interfaces adopt linear and zigzag configurations for the ZnO($10\bar{1}0$) and ($11\bar{2}0$) surfaces, respectively. These particular patterns are due to the arrangement of the negatively charged O ions at the interfaces (Figure 2c,f). These results

show that although there is a net charge transfer from ZnO to the Au NP, Au atoms at the interface can be positively or negatively charged.

4.4. Encapsulation of Au by ZnO. As discussed in Section 2, experimental studies have shown that Au NPs can become encapsulated by ZnO by annealing in the presence of oxygen. Zn interstitials are a common defect in ZnO and also are predicted to have fairly low barriers to diffusion (0.2−0.3 eV).[70] Therefore, one possible mechanism for ZnO encapsulation is the diffusion of Zn interstitials from the support to the surface where they could react with O$_2$ to form ZnO monomers. To explore the feasibility of this mechanism, we assess the stability of interstitials in various positions within the slab both in O-poor and O-rich conditions. We first introduce a neutral Zn interstitial in the four different sites

shown in Figure 6 and assess stability in the O-poor condition. Site A is the interstitial in bulk ZnO for which by definition the
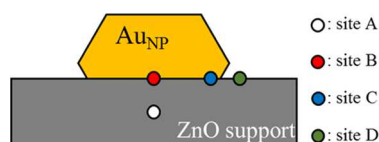

Figure 6. Four different sites for the Zn interstitial. Site A is in bulk. Site B and C are at the center and edge of the interface between Au NPs and ZnO support. Site D is just outside the perimeter of the Au NPs.

segregation energy is zero. Sites B and C are interstitial sites at the interface between the Au NPs and ZnO support. The former is in the middle and the latter at the edge of the NP. Finally, site D is just outside the perimeter of the Au NP. We computed the segregation energy of the interstitial at these four sites for NPs on both ZnO surfaces to assess their relative stability (shown in Table 6). The results indicate that the

Table 6. Segregation Energy for the Zn Interstitial to Different Sites in the Au NP/ZnO System (see Figure 6)

	segregation energy (eV)			
supports	site A	site B	site C	site D
$ZnO(10\bar{1}0)$	0.0	−3.2	−4.9	−4.8
$ZnO(11\bar{2}0)$	0.0	−2.5	−2.9	−2.4

interstitial prefers segregation to the Au/ZnO interface but with a preference for sites near the perimeter of the NP. We note that the electronic properties of the Zn interstitial in the bulk and Au/ZnO interface systems are different. The former is doubly ionized with two electrons delocalized in the ZnO conduction band, whereas in the latter case, the electrons are transferred to Au since the Fermi energy lies within the ZnO band gap. As a result, the absolute formation energy is correspondingly reduced.

To assess stability in an O-rich environment, we introduce an additional O atom into the system. We consider two configurations for each ZnO support. One has the Zn interstitial in site C. The second has the Zn interstitial in site D with an oxygen atom added (supplied by an oxygen molecule) forming a ZnO monomer. The optimized structures of the former and latter configurations are shown in the top and bottom panels of Figure 7. The total energy differences between the two configurations are −2.1 and −1.2 eV, respectively (i.e., ZnO formation is thermodynamically favorable in O-rich conditions). The energy of the oxygen atom is taken as half the total energy of an oxygen molecule. One could also consider that a dissociated oxygen atom may be present on the Au NP (as a result of the CO oxidation reaction, for example). The formation energies, in this case, are −1.1 and −0.8 eV (see Figure S1 in the Supporting Information). The bond length of the ZnO monomer is approximately 2.0 Å, which is similar to the bond length in wurtzite ZnO. The segregation energy for a Zn interstitial to the bare ZnO surface is much smaller than at the NP perimeter (−0.55 eV for both the $ZnO(10\bar{1}0)$ and $ZnO(11\bar{2}0)$ surfaces). Therefore, we predict that the formation of ZnO at the perimeter of the Au NPs to be more favorable than the formation of ZnO islands.
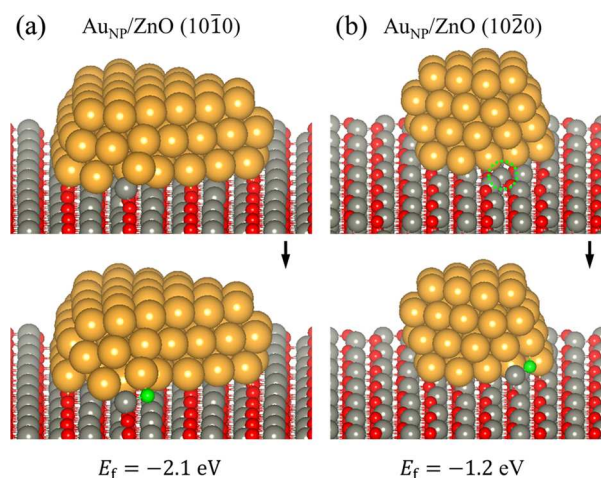

Figure 7. Atomic structure for supported Au NPs in the presence of an additional adsorbed oxygen atom (provided by an oxygen molecule). (a) Au NP supported on $ZnO(10\bar{1}0)$ and (b) Au NP supported on $ZnO(10\bar{2}0)$. (top) Configurations with a Zn interstitial at site C. (bottom) Configuration with the Zn interstitial in site D forming a ZnO monomer with an adsorbed O atom. The green-dashed circle (in the top (b)) highlights the partially obscured Zn atom at the interface between the Au NP and $ZnO(11\bar{2}0)$ surfaces. Atoms are colored as in previous figures. The additional adsorbed O atom is represented by a green sphere.

The above calculations indicate that the presence of Zn interstitials can lead to the formation of ZnO near the perimeter of the Au NPs in O-rich conditions. Further segregation, diffusion, and reaction could lead to a number of different scenarios such as the association of ZnO monomers into chains, growth of ZnO on the Au facets, or the formation of a ZnO film at the Au/ZnO interface. Since the formation of bulk ZnO is most favorable thermodynamically, the growth of thick ZnO encapsulation layers on Au or the formation of a ZnO film at the Au/ZnO interface is likely to be the most stable options. However, kinetic factors will likely play an important role in determining how the structure evolves in this high nonequilibrium process.

4.5. O₂ Adsorption on ZnO-Supported Au Nanoparticles. We next systematically adsorb O_2 molecules at different sites on the supported Au NPs and calculate the corresponding adsorption energy E_{ads}. We note that the PBE XC functional we employ has been shown in previous studies to be reliable for general trends in molecular oxygen adsorption.[63,71] Figure 8 shows the stable configurations of molecular oxygen adsorbed on ZnO-supported Au NPs. There are four types of stable configurations found in our calculations: (I) O_2 molecules adsorbed on top of Au atoms on (001) facets, (II) dissociative adsorption at bridge sites on the (001) facet, (III) O_2 molecule adsorption between the perimeter of Au particles and an atom from the support, and (IV) O_2 molecule adsorption between a ZnO monomer formed at the NP perimeter and the Au NP. The presence of ZnO monomers at the perimeter may be a transient feature as the system evolves (e.g., toward full or partial encapsulation of the particle by ZnO). Bond lengths (l) are shown in the figures for specific atom pairs. l_{O-O} is the distance between adsorbed O atoms, whereas other bond lengths are between the adsorbed O atoms and adjacent atoms (such as Au and Zn atoms). Adsorption types I, III, and IV involve molecular adsorption with $l_{O-O} \sim 1.3$ Å, which is slightly greater than in
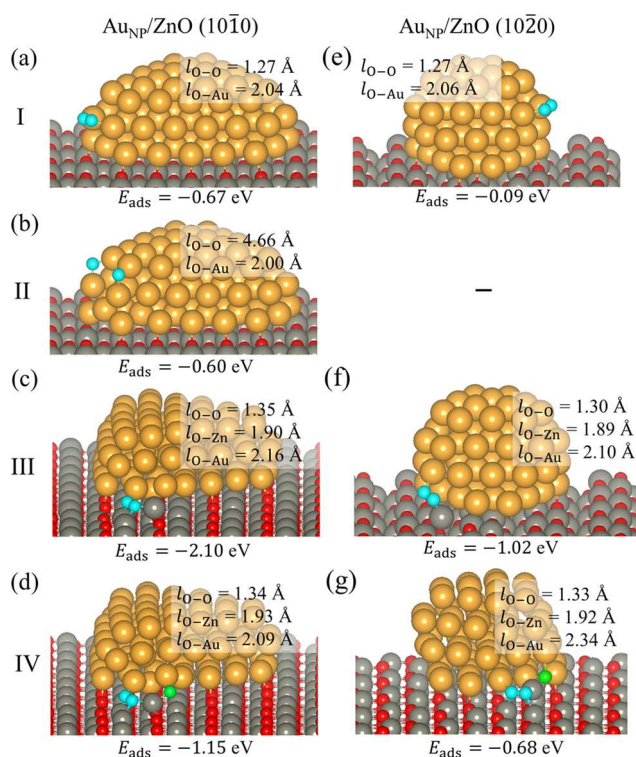
Figure 8. Adsorption energy and atomic configuration of molecular oxygen adsorbed on ZnO-supported Au nanoparticles. (a−d) Atomic structures of O_2 molecules adsorbed on Au NPs supported on ZnO($10\bar{1}0$). (e−g) Atomic structures of O_2 molecules adsorbed on Au NPs supported on ZnO($11\bar{2}0$). Both highlight the different types of adsorption (labeled I−IV). Atoms are colored as in previous figures. The blue spheres represent the adsorbed O_2 molecule.

the gas phase ($l_{O-O} = 1.1$ Å). Type II adsorption is dissociative leaving O atoms adsorbed on the bridge sites of the Au(001) facet with $l_{O-O} \sim 4.7$ Å. The O−Au bond length for all sites is in the range from 2.0 to 2.3 Å. The adsorption energies for type I and II are comparable even though the adsorption sites and geometries are very different. A similar effect has been observed for oxygen adsorption on MgO-supported Au NPs.[55]

Bader analysis shows that the Au atoms adjacent to the O_2 molecule transfer around 0.3 electrons to the molecule. In the case of type II adsorption, the charge transfer increases to around 0.8 electrons. The charge transfer shows a good agreement with the recent work.[72] The Zn atoms (in type III and IV sites) transfer around 1.0−1.2 electrons to the dissociatively adsorbed of O atoms, giving a similar charge state to that of an O atom in bulk ZnO (−1.4 e). The Zn atom and the Au atom transfer 0.7 and 0.6 electrons to the molecular O atoms. The adsorption energies shown in Figure 8c,d,f,g demonstrate that the ZnO monomer (or the Zn atom) provides slightly better ability to capture the O_2 molecule. The large size of our models (around 600 atoms) and the many possible reactions pathways mean that a full study of CO reactivity would be computationally prohibitive. We note, however, that the preference for oxygen adsorption at the perimeter (type III and IV) as well as the presence of dissociatively adsorbed oxygen molecules (type II) are likely to play an important role in reactivity.

5. DISCUSSION AND CONCLUSIONS

Several factors may influence the accuracy of our predictions that warrant some discussion. First, the NLEP + U method is an empirical approach fitted to the experimental parameters (such as the lattice constant and band gap). Although the formation enthalpy and surface formation energy of bulk ZnO are consistent with the experimental observation and hybrid calculation, we found that the work functions of wurtzite ZnO and fcc Au predicted by the GGA + NLEP + U calculation are not in the correct order. The exact difference of work function between ZnO and Au should be 0.62 eV, but the calculated difference is −0.76 eV. Due to the nonlinear correlation between work function and NLEP parameters, it is difficult to find parameters that describe all properties accurately. An accurate calculation of work functions of metals and oxides using a consistent approach is very challenging. Standard GGA may underestimate the ZnO ionization potential, and hybrid functionals are likely to be more appropriate. However, hybrid functionals will give poor results for the metal. The GGA + NLEP + U approach is a compromise, which provides reasonable electronic properties for Au and ZnO while being computationally cheap enough for calculations on systems with up to 600 atoms. This approximation may lead to some inaccuracy in the position of the Au Fermi energy, which may affect predictions of charge transfer between Au and ZnO but should not affect any of our main conclusions.

In Section 4.2, we predicted the shape of Au NPs by computing the adhesion energy between stoichiometric Au and ZnO slabs. Although a global cluster optimization is beyond the scope of this study, we note that the structure of Au NPs can be sensitive to the approximations employed[73−75] particularly for small NP sizes. The size of NPs in the experimental Au/ZnO catalysts is around 5 nm where one should expect truncated-octahedral shapes to dominate. The simulated Au NPs are approximately 2 nm in size due to computational limitations. However, the predicted morphologies are similar to those found in experimental TEM images.[26] The presence of Zn-rich ZnO surfaces due to the segregation of Zn interstitials may also influence the equilibrium shape of supported Au NPs. To address this point, we computed adhesion energies in the presence of Zn interstitials and found that adhesion energies can be increased further for Zn-rich interfaces (see Table S1 in the Supporting Information). In this case, the predicted height of the Au NPs would be correspondingly reduced, but the shape is unchanged qualitatively.

The other main factor affecting accuracy is the limited number of oxygen adsorption configurations considered. Possible adsorption configurations are obtained by a systematic investigation, but the real situation may involve more varied modes of adsorption. Molecular dynamics simulation could be an alternative approach to model the adsorption to obtain more possible configurations, but the huge computational cost makes it currently unfeasible. O_2 and CO adsorption and dissociation may, in practice, include many intermediate steps, such as O atom diffusion. Indeed, many recent works already provided many constructive results on the transition barriers for CO oxidation.[63,64,71] Although the precise dynamics of O atoms during CO oxidation on Au NPs supported on ZnO surface is beyond the scope of this work, we can still provide some useful insights into reactivity.

In summary, we have investigated the morphology of Au NPs using the formation energies of low-index Au surfaces and the adhesion energy of interfaces between Au and ZnO surfaces. The morphology of the free Au NP is truncated-octahedral, whereas the morphology of the supported Au NP can involve three different orientations normal to the ZnO surface: (001), (110), and (111). The calculated adhesion energies show that the interface between Au(111) and ZnO($10\bar{1}0$) is the most energetically stable with E_{ad} = 0.8 J m^{-2}. The interstitial in ZnO is energetically stable and can lead to the growth of ZnO around the Au NPs in O-rich conditions. Overall, this study provides atomistic insight into the structure and properties of ZnO-supported Au NPs relevant for CO oxidation.

■ ASSOCIATED CONTENT

Ⓢ Supporting Information

The Supporting Information is available free of charge on the ACS Publications website at DOI: 10.1021/acs.jpcc.9b02639.

Au/ZnO adhesion energies with different concentrations of Zn interstitials segregated to the Au/ZnO interface (Table S1) and atomic structures of supported Au NPs in the presence of an additional adsorbed oxygen atom (Figure S1) (PDF)

■ AUTHOR INFORMATION

Corresponding Authors
*E-mail: sh1635@york.ac.uk (S.-H.H.).
*E-mail: keith.mckenna@york.ac.uk (K.M.).

ORCID Ⓘ
Shih-Hsuan Hung: 0000-0001-8925-8945
Keith McKenna: 0000-0003-0975-3626

Notes
The authors declare no competing financial interest.

■ ACKNOWLEDGMENTS

■ REFERENCES

(1) Valden, M.; Lai, X.; Goodman, D. W. Onset of catalytic activity of gold clusters on titania with the appearance of nonmetallic properties. *Sci.* **1998**, *281*, 1647–1650.

(2) Wang, Z.; Fu, H.; Tian, Z.; Han, D.; Gu, F. Strong metal-support interaction in novel core-shell Au-CeO$_2$ nanostructures induced by different pretreatment atmospheres and its influence on CO oxidation. *Nanoscale* **2016**, *8*, 5865–5872.

(3) Ha, H.; An, H.; Yoo, M.; Lee, J.; Kim, H. Y. Catalytic CO oxidation by CO-saturated Au nanoparticles supported on CeO$_2$: Effect of CO coverage. *J. Phys. Chem. C* **2017**, *121*, 26895–26902.

(4) Tang, H.; Wei, J.; Liu, F.; Qiao, B.; Pan, X.; Li, L.; Liu, J.; Wang, J.; Zhang, T. Strong metal-support interactions between gold nanoparticles and nonoxides. *J. Am. Chem. Soc.* **2016**, *138*, 56–59.

(5) Liu, J.; Qiao, B.; Song, Y.; Tang, H.; Huang, Y.; Liu, J. Highly active and sintering-resistant heteroepitaxy of Au nanoparticles on ZnO nanowires for CO oxidation. *J. Energy Chem.* **2016**, *25*, 361–370.

(6) Carabineiro, S.; Machado, B.; Bacsa, R.; Serp, P.; Drai, G.; Faria, J.; Figueiredo, J. Catalytic performance of Au/ZnO nanocatalysts for CO oxidation. *J. Catal.* **2010**, *273*, 191–198.

(7) Fageria, P.; Gangopadhyay, S.; Pande, S. Synthesis of ZnO/Au and ZnO/Ag nanoparticles and their photocatalytic application using UV and visible light. *RSC Adv.* **2014**, *4*, 24962–24972.

(8) Li, P.; Wei, Z.; Wu, T.; Peng, Q.; Li, Y. Au-ZnO hybrid nanopyramids and their photocatalytic properties. *J. Am. Chem. Soc.* **2011**, *133*, 5660–5663.

(9) Wang, Q.; Geng, B.; Wang, S. ZnO/Au hybrid nano-architectures: Wet-chemical synthesis and structurally enhanced photocatalytic performance. *Environ. Sci. Technol.* **2009**, *43*, 8968–8973.

(10) Milone, C.; Crisafulli, C.; Ingoglia, R.; Schipilliti, L.; Galvagno, S. A comparative study on the selective hydrogenation of α, β unsaturated aldehyde and ketone to unsaturated alcohols on Au supported catalysts. *Catal. Today* **2007**, *122*, 341–351.

(11) Bailie, J. E.; Abdullah, H. A.; Anderson, J. A.; Rochester, C. H.; Richardson, N. V.; Hodge, N.; Zhang, J.-G.; Burrows, A.; Kiely, C. J.; Hutchings, G. J. Hydrogenation of but-2-enal over supported Au/ZnO catalysts. *Phys. Chem. Chem. Phys.* **2001**, *3*, 4113–4121.

(12) Castillejos, E.; Gallegos-Suarez, E.; Bachiller-Baeza, B.; Bacsa, R.; Serp, P.; Guerrero-Ruiz, A.; Rodríguez-Ramos, I. Deposition of gold nanoparticles on ZnO and their catalytic activity for hydro-genation applications. *Catal. Commun.* **2012**, *22*, 79–82.

(13) Milone, C.; Ingoglia, R.; Pistone, G. A.; Neri; Galvagno, S. Activity of gold catalysts in the liquid-phase oxidation of O-hydroxybenzyl alcohol. *Catal. Lett.* **2003**, *87*, 201–209.

(14) Zhang, X.; Liu, Y.; Kang, Z. 3D branched ZnO nanowire arrays decorated with plasmonic Au nanoparticles for high-performance photoelectrochemical water splitting. *ACS Appl. Mater. Interfaces* **2014**, *6*, 4480–4489.

(15) Pawinrat, P.; Mekasuwandumrong, O.; Panpranot, J. Synthesis of Au-ZnO and Pt-ZnO nanocomposites by one-step flame spray pyrolysis and its application for photocatalytic degradation of dyes. *Catal. Commun.* **2009**, *10*, 1380–1385.

(16) Yang, T.-H.; Huang, L.-D.; Harn, Y.-W.; Lin, C.-C.; Chang, J.-K.; Wu, C.-I.; Wu, J.-M. High density unaggregated Au nanoparticles on ZnO nanorod arrays function as efficient and recyclable photocatalysts for environmental purification. *Small* **2013**, *9*, 3169–3182.

(17) Wang, Z. L. Zinc oxide nanostructures: Growth, properties and applications. *J. Phys.: Condens. Matter* **2004**, *16*, R829–R858.

(18) Montenegro, D.; Souissi, A.; Martínez-Tomás, C.; Muñoz-Sanjosé, V.; Sallet, V. Morphology transitions in ZnO nanorods grown by MOCVD. *J. Cryst. Growth* **2012**, *359*, 122–128.

(19) Elias, J.; Tena-Zaera, R.; Lévy-Clément, C. Electrodeposition of ZnO nanowires with controlled dimensions for photovoltaic applications: Role of buffer layer. *Thin Solid Films* **2007**, *515*, 8553–8557.

(20) Yu, J.; Huang, B.; Qin, X.; Zhang, X.; Wang, Z.; Liu, H. Hydrothermal synthesis and characterization of ZnO films with different nanostructures. *Appl. Surf. Sci.* **2011**, *257*, 5563–5565.

(21) Rivera, A.; Zeller, J.; Sood, A.; Anwar, M. A comparison of ZnO nanowires and nanorods grown using MOCVD and hydrothermal processes. *J. Electron. Mater.* **2013**, *42*, 894–900.

(22) Liu, B.; Zeng, H. C. Room temperature solution synthesis of monodispersed single-crystalline ZnO nanorods and derived hier-archical nanostructures. *Langmuir* **2004**, *20*, 4196–4204.

(23) Rusdi, R.; Rahman, A. A.; Mohamed, N. S.; Kamarudin, N.; Kamarulzaman, N. Preparation and band gap energies of ZnO

nanotubes, nanorods and spherical nanostructures. *Powder Technol.* **2011**, *210*, 18−22.

(24) Bao, Z.; Yuan, Y.; Leng, C.; Li, L.; Zhao, K.; Sun, Z. One-pot synthesis of noble metal/zinc oxide composites with controllable morphology and high catalytic performance. *ACS Appl. Mater. Interfaces* **2017**, *9*, 16417−16425.

(25) Castillejos, E.; Bacsa, R.; Guerrero-Ruiz, A.; Rodríguez-Ramos, I.; Datas, L.; Serp, P. Catalytic activity of gold supported on ZnO tetrapods for the preferential oxidation of carbon monoxide under hydrogen rich conditions. *Nanoscale* **2011**, *3*, 929−932.

(26) Liu, X.; Liu, M.-H.; Luo, Y.-C.; Mou, C.-Y.; Lin, S. D.; Cheng, H.; Chen, J.-M.; Lee, J.-F.; Lin, T.-S. Strong metal-support interactions between gold nanoparticles and ZnO nanorods in CO oxidation. *J. Am. Chem. Soc.* **2012**, *134*, 10251−10258.

(27) Wang, H.; Li, M.; Jia, L.; Li, L.; Wang, G.; Zhang, Y.; Li, G. Surfactant-assisted in situ chemical etching for the general synthesis of ZnO nanotubes array. *Nanoscale Res. Lett.* **2010**, *5*, 1102.

(28) Hung, S.-H.; McKenna, K. First-principles prediction of the morphology of $L1_0$ FePt nanoparticles supported on Mg(Ti)O for heat-assisted magnetic recording applications. *Phys. Rev. Mater.* **2017**, *1*, No. 024405.

(29) Reeber, R. R. Lattice parameters of ZnO from 4.2 to 296 K. *J. Appl. Phys.* **1970**, *41*, 5063−5066.

(30) Sernelius, B. E.; Berggren, K.-F.; Jin, Z.-C.; Hamberg, I.; Granqvist, C. G. Band-gap tailoring of ZnO by means of heavy Al doping. *Phys. Rev. B* **1988**, *37*, 10244.

(31) Look, D. C.; Hemsky, J. W.; Sizelove, J. R. Residual native shallow donor in ZnO. *Phys. Rev. Lett.* **1999**, *82*, 2552−2555.

(32) Erhart, P.; Klein, A.; Albe, K. First-principles study of the structure and stability of oxygen defects in zinc oxide. *Phys. Rev. B* **2005**, *72*, No. 085213.

(33) Pala, R. G. S.; Metiu, H. Modification of the oxidative power of ZnO (10$\bar{1}$0) surface by substituting some surface Zn atoms with other metals. *J. Phys. Chem. C* **2007**, *111*, 8617−8622.

(34) Meyer, B.; Marx, D. Density-functional study of the structure and stability of ZnO surfaces. *Phys. Rev. B* **2003**, *67*, No. 035403.

(35) Erhart, P.; Albe, K.; Klein, A. First-principles study of intrinsic point defects in ZnO: Role of band structure, volume relaxation, and finite-size effects. *Phys. Rev. B* **2006**, *73*, No. 205203.

(36) Oba, F.; Togo, A.; Tanaka, I.; Paier, J.; Kresse, G. Defect energetics in ZnO: A hybrid Hartree-Fock density functional study. *Phys. Rev. B* **2008**, *77*, No. 245202.

(37) Vlasenko, L. S.; Watkins, G. D. Optical detection of electron paramagnetic resonance in room-temperature electron-irradiated ZnO. *Phys. Rev. B* **2005**, *71*, No. 125210.

(38) Vanheusden, K.; Seager, C.; Warren, W.; Tallant, D.; Voigt, J. Correlation between photoluminescence and oxygen vacancies in ZnO phosphors. *Appl. Phys. Lett.* **1996**, *68*, 403−405.

(39) Hutson, A. R. Hall effect studies of doped zinc oxide single crystals. *Phys. Rev.* **1957**, *108*, 222−230.

(40) Janotti, A.; Van de Walle, C. G. Oxygen vacancies in ZnO. *Appl. Phys. Lett.* **2005**, *87*, No. 122102.

(41) Lany, S.; Zunger, A. Accurate prediction of defect properties in density functional supercell calculations. *Model. Simul. Mater. Sci. Eng.* **2009**, *17*, No. 084002.

(42) Christensen, N. E. Electronic structure of GaAs under strain. *Phys. Rev. B* **1984**, *30*, 5753−5765.

(43) Wang, L.-W. Large-scale local-density-approximation band gap-corrected GaAsN calculations. *Appl. Phys. Lett.* **2001**, *78*, 1565−1567.

(44) Lany, S.; Raebiger, H.; Zunger, A. Magnetic interactions of Cr−Cr and Co−Co impurity pairs in ZnO within a band-gap corrected density functional approach. *Phys. Rev. B* **2008**, *77*, No. 241201.

(45) Kaneti, Y. V.; Zhang, Z.; Yue, J.; Zakaria, Q. M.; Chen, C.; Jiang, X.; Yu, A. Crystal plane-dependent gas-sensing properties of zinc oxide nanostructures: Experimental and theoretical studies. *Phys. Chem. Chem. Phys.* **2014**, *16*, 11471−11480.

(46) Ntep, J.-M.; Barbé, M.; Cohen-Solal, G.; Bailly, F.; Lusson, A.; Triboulet, R. ZnO growth by chemically assisted sublimation. *J. Cryst. Growth* **1998**, *184−185*, 1026−1030.

(47) Skompska, M.; Zarębska, K. Electrodeposition of ZnO nanorod arrays on transparent conducting substrates-a review. *Electrochim. Acta* **2014**, *127*, 467−488.

(48) Li, Q.; Yin, D.; Li, J.; Deepak, F. L. Atomic-scale understanding of gold cluster growth on different substrates and adsorption-induced structural change. *J. Phys. Chem. C* **2018**, *122*, 1753−1760.

(49) Zhan, W.; Shu, Y.; Sheng, Y.; Zhu, H.; Guo, Y.; Wang, L.; Guo, Y.; Zhang, J.; Lu, G.; Dai, S. Surfactant-assisted stabilization of Au colloids on solids for heterogeneous catalysis. *Angew. Chem.* **2017**, *129*, 4565−4569.

(50) Zhou, Y.; Zhu, Y.; Wang, Z.-Q.; Zou, S.; Ma, G.; Xia, M.; Kong, X.; Xiao, L.; Gong, X.-Q.; Fan, J. Catalytic activity control via crossover between two different microstructures. *J. Am. Chem. Soc.* **2017**, *139*, 13740−13748.

(51) Singh-Miller, N. E.; Marzari, N. Surface energies, work functions, and surface relaxations of low-index metallic surfaces from first principles. *Phys. Rev. B* **2009**, *80*, No. 235407.

(52) Benoit, M.; Langlois, C.; Combe, N.; Tang, H.; Casanove, M.-J. Structural and electronic properties of the Au(001)/Fe(001) interface from density functional theory calculations. *Phys. Rev. B* **2012**, *86*, No. 075460.

(53) Barnard, A. S.; Lin, X.; Curtiss, L. A. Equilibrium morphology of face-centered cubic gold nanoparticles >3 nm and the shape changes induced by temperature. *J. Phys. Chem. B* **2005**, *109*, 24465−24472.

(54) Kuwauchi, Y.; Yoshida, H.; Akita, T.; Haruta, M.; Takeda, S. Intrinsic catalytic structure of gold nanoparticles supported on TiO_2. *Angew. Chem., Int. Ed.* **2012**, *51*, 7729−7733.

(55) Molina, L. M.; Hammer, B. Theoretical study of CO oxidation on Au nanoparticles supported by MgO(100). *Phys. Rev. B* **2004**, *69*, No. 155424.

(56) Tauster, S. Strong metal-support interactions. *Acc. Chem. Res.* **1987**, *20*, 389−394.

(57) Qin, Z.-H.; Lewandowski, M.; Sun, Y.-N.; Shaikhutdinov, S.; Freund, H.-J. Encapsulation of Pt nanoparticles as a result of strong metal-support interaction with Fe_3O_4 (111). *J. Phys. Chem. C* **2008**, *112*, 10209−10213.

(58) Pan, C.-J.; Tsai, M.-C.; Su, W.-N.; Rick, J.; Akalework, N. G.; Agegnehu, A. K.; Cheng, S.-Y.; Hwang, B.-J. Tuning/exploiting strong metal-support interaction (SMSI) in heterogeneous catalysis. *J. Taiwan Inst. Chem. Eng.* **2017**, *74*, 154−186.

(59) Mills, G.; Gordon, M. S.; Metiu, H. The adsorption of molecular oxygen on neutral and negative Au_n clusters (n = 2−5). *Chem. Phys. Lett.* **2002**, *359*, 493−499.

(60) Ding, X.; Li, Z.; Yang, J.; Hou, J.; Zhu, Q. Adsorption energies of molecular oxygen on Au clusters. *J. Chem. Phys.* **2004**, *120*, 9594−9600.

(61) Xu, Y.; Mavrikakis, M. Adsorption and dissociation of O_2 on gold surfaces: Effect of steps and strain. *J. Phys. Chem. B* **2003**, *107*, 9298−9307.

(62) Yoon, B.; Häkkinen, H.; Landman, U. Interaction of O_2 with gold clusters: Molecular and dissociative adsorption. *J. Phys. Chem. A* **2003**, *107*, 4066−4071.

(63) Guo, N.; Lu, R.; Liu, S.; Ho, G. W.; Zhang, C. High catalytic activity of Au clusters supported on ZnO nanosheets. *J. Phys. Chem. C* **2014**, *118*, 21038−21041.

(64) Duan, Y.; Li, Z.; Li, Y.; Zhang, Y.; Li, L.; Li, J. New insight of the Mars-van Krevelen mechanism of the CO oxidation by gold catalyst on the ZnO(101) surface. *Comput. Theor. Chem.* **2017**, *1100*, 28−33.

(65) Kresse, G.; Furthmüller, J. Efficient iterative schemes for ab initio total-energy calculations using a plane-wave basis set. *Phys. Rev. B* **1996**, *54*, 11169−11186.

(66) Blöchl, P. E. Projector augmented-wave method. *Phys. Rev. B* **1994**, *50*, 17953−17979.

(67) Perdew, J. P.; Burke, K.; Ernzerhof, M. Generalized gradient approximation made simple. *Phys. Rev. Lett.* **1996**, *77*, 3865−3868.

(68) Usuda, M.; Hamada, N.; Kotani, T.; van Schilfgaarde, M. All-electron GW calculation based on the LAPW method: Application to wurtzite ZnO. *Phys. Rev. B* **2002**, *66*, No. 125101.

(69) Henkelman, G.; Arnaldsson, A.; Jónsson, H. A fast and robust algorithm for Bader decomposition of charge density. *Comput. Mater. Sci.* **2006**, *36*, 354−360.

(70) Erhart, P.; Albe, K. Diffusion of zinc vacancies and interstitials in zinc oxide. *Appl. Phys. Lett.* **2006**, *88*, No. 201918.

(71) Lopez, N.; Nørskov, J. K. Catalytic CO oxidation by a gold nanoparticle: A density functional study. *J. Am. Chem. Soc.* **2002**, *124*, 11262−11263.

(72) Mahata, A.; Bhauriyal, P.; Rawat, K. S.; Pathak, B. Pt_3Ti (Ti_{19}@Pt_{60})-based cuboctahedral core-shell nanocluster favors a direct over indirect oxygen reduction reaction. *ACS Energy Lett* **2016**, *1*, 797−805.

(73) Barnard, A. S.; Curtiss, L. A. predicting the shape and structure of face-centered cubic gold nanocrystals smaller than 3 nm. *ChemPhysChem* **2006**, *7*, 1544−1553.

(74) Barnard, A. Modelling of nanoparticles: approaches to morphology and evolution. *Rep. Prog. Phys.* **2010**, *73*, No. 086502.

(75) McKenna, K. P. Gold nanoparticles under gas pressure. *Phys. Chem. Chem. Phys.* **2009**, *11*, 4145−4151.